Microwave Photonic MIMO Radar for High-Resolution Imaging

Bindong Gao, Fangzheng Zhang ⦿, *Senior Member, IEEE*, Guanqun Sun ⦿, Yu Xiang, and Shilong Pan ⦿, *Senior Member, IEEE, Fellow, OSA*

Abstract—**A microwave photonic multiple-input and multiple-output (MIMO) radar is proposed and demonstrated to implement high-resolution imaging. In the proposed system, multiple orthogonal linearly frequency modulated (LFM) signals are generated by heterodyning between two optical frequency combs, which enables a MIMO transmitting array with a simple and reconfigurable structure. The receiving array uses photonic frequency mixing to implement multiple channel separation and de-chirp processing simultaneously. This microwave photonic MIMO radar can have a large operation bandwidth and a large equivalent aperture, which helps to achieve high-resolution imaging in both range and azimuth directions. In the experiment, a microwave photonic 4 × 8 MIMO radar is established with a 2-GHz bandwidth in each channel. Based on this MIMO radar, high-resolution back-projection (BP) imaging with a theoretical range resolution of 7.5 cm and azimuth resolution of 1.85° is demonstrated. The experimental results can verify the feasibility of the proposed MIMO radar, which is a good solution to high-resolution radar imaging by combining microwave photonic and MIMO technologies.**

Index Terms—**Microwave photonics, back-projection (BP) imaging, linearly frequency modulation (LFM), multiple-input and multiple-output (MIMO), radar.**

I. INTRODUCTION

MICROWAVE photonic (MWP) technology enables the generation and processing of high-frequency and broadband microwave signals [1]–[3], which is particularly favorable to improve the range resolution of radar systems [4]–[6]. In recent years, several microwave photonic monostatic radars have been reported for high-resolution synthetic aperture imaging [7]–[12], in which the range resolution reaches sub-centimeter levels [13]. To achieve a high azimuth resolution, a certain observation time is usually required to form a large synthetic aperture, which lowers the processing speed and makes it difficult for imaging fast-moving targets. What's more, as the range resolution is dramatically improved, complicated motion compensations are required to construct high-precision synthetic aperture radar images [14], which further complicates the computations and reduces the imaging speed. Fortunately, the radar azimuth resolution can be improved by using array radars [15], which can avoid or reduce the time integration and achieve fast or even snapshot imaging. Previously, a broadband microwave photonic phased array radar imaging with digital beamforming (DBF) is demonstrated in [16], whereas the azimuth resolution is still limited by the scale of the radar array. A promising solution to this problem is to use the multiple-input and multiple-output (MIMO) radar architecture, which can achieve a large equivalent aperture with a small number of array elements [17].

Recently, a few microwave photonic distributed MIMO radars have been proposed to enable a large operation bandwidth and/or to expand the equivalent aperture size [18]–[20]. In [18], radio frequency (RF) up- and down-conversion using optical frequency combs are demonstrated to generate multiple transmit signals and process the radar echoes, respectively. In the experimental demonstration, a dual-band 2 × 4 MIMO radar with a bandwidth of 400 MHz is established, and the azimuth resolution is greatly improved with coherent MIMO processing. In [19], a wideband microwave photonic distributed coherent aperture radar (DCAR) was proposed, in which photonic digital-to-analog converters are used to generate wideband radar signals, and a fiber-connected network is adopted to expand the equivalent aperture size. This DCAR was proved to have a high signal-to-noise ratio (SNR) gain thanks to the coherent accumulation. Additionally, a microwave photonic distributed MIMO radar based on wavelength division multiplexing and time-interleaved receiving was reported in [20], based on which 3D radar imaging is demonstrated. In addition to the distributed MIMO radar, microwave photonic collocated MIMO radars have also been demonstrated. In [21], a broadband microwave photonic collocated MIMO radar was proposed with a wavelength division multiplexing architecture. In this system, photonic frequency multiplication is applied to generate multiple orthogonal radar waveforms, and photonic frequency mixing is implemented to perform de-chirp processing and separate the multiple channels simultaneously. Based on this configuration, a 2 × 2 MIMO radar with a bandwidth of 4 GHz is demonstrated for high precise direction-of-arrival estimation. Recently, a microwave photonic MIMO radar with 16 transmitters and 16 receivers was demonstrated in [22]. This system uses optical delay lines to
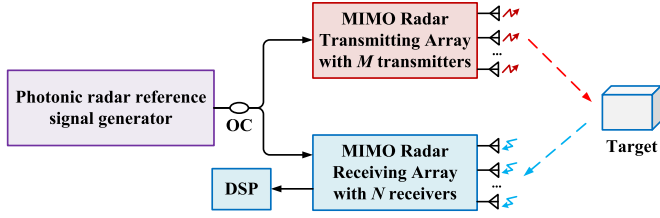
Fig. 1. The overall structure of the proposed microwave photonic MIMO radar system. (OC: Optical coupler, DSP: Digital signal processing)

process time-division orthogonal signals, and the 3D near field imaging is successfully demonstrated.

In this paper, we propose a microwave photonic collocated MIMO radar and demonstrate its application in high-resolution imaging. In the transmitting array, multiple orthogonal linear frequency modulation (LFM) signals are generated by heterodyning between two optical frequency combs, which not only leads to a simplified structure compared with most of the previous photonic MIMO radars but also guarantees a good coherence between different channels. In the receiving array, photonic frequency mixing is implemented for separation and de-chirp processing of the radar echoes from different channels. In the experiment, the feasibility of the proposed microwave photonic MIMO radar system is verified through a 4×8 MIMO radar system with a 2-GHz bandwidth in each channel. Based on the established system, high-resolution back-projection (BP) radar imaging is also demonstrated.

This paper is organized as follows. The configuration and principle of the proposed microwave photonic MIMO radar are introduced in Section II. An experiment is carried out in Section III, which demonstrates the feasibility of the proposed radar system and shows the high-resolution imaging results. Finally, a conclusion is drawn in Section IV.

II. MICROWAVE PHOTONIC MIMO RADAR SYSTEM

Fig. 1 shows the structure of the proposed microwave photonic MIMO radar, which works in a frequency division multiplexing mode by transmitting multiple orthogonal LFM signals in different ranges. It is composed of four parts, i.e., the photonic radar reference signal generator, the MIMO radar transmitting array, the MIMO radar receiving array, and the digital signal processing (DSP) unit. In the photonic radar reference signal generator, an optical frequency comb with fixed comb-line spacing and an optical frequency-swept comb are used to generate multiple optical sideband pairs. The obtained reference signal is divided into two branches. The signal in one branch is sent to the MIMO radar transmitting array to generate M orthogonal LFM signals with different central frequencies, and the signal in the other branch is used as the reference of the MIMO radar receiving array. The M orthogonal radar echoes are collected by N receiving antennas, and $M \times N$ de-chirped signals are obtained and sampled after photonics-based frequency mixing. Finally, the $M \times N$ de-chirped signals are processed in the DSP unit to construct the image of the targets. The detailed implementation and principle of the proposed MIMO radar are introduced in what follows.
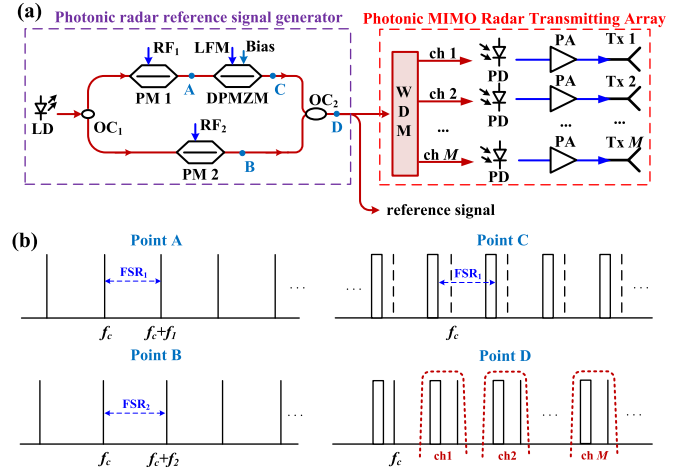

Fig. 2. (a) The structure of the photonic radar reference signal generator and the photonic MIMO radar transmitting array. LD: Laser diode, PM: Phase modulator, DPMZM: Dual-parallel Mach Zehnder modulator, WDM: Wavelength division multiplexer, RF: Radio frequency signal, LFM: Linear frequency-modulation signal, PD: Photodetector, PA: Power amplifier, Tx: Transmitting antenna, and (b) Illustration of the optical spectra at different points. FSR: Free spectral range.

A. Photonics-Based MIMO Radar Signal Generation

Fig. 2(a) shows the schematic diagram of the photonic radar reference signal generator and the photonic MIMO radar transmitting array. The photonic radar reference signal generator consists of a laser diode (LD), two phase modulators (PM), a dual-parallel Mach Zehnder modulator (DPMZM), and two optical couplers (OC). The light generated by the LD is firstly divided into two branches by an optical coupler (OC1) and modulated by two PMs, respectively. The two PMs (PM1 and PM2) are driven by two radio frequency signals with different frequencies (f_1 and f_2). After the PMs, two optical frequency combs with different free spectral range (FSR) are obtained (point A and point B in Fig. 2(b)), which can be expressed as:

$$E_{PM1} = \sum_{i=0}^{\infty} A_i e^{j2\pi(f_c \pm i \cdot f_1)t} \quad (1)$$

$$E_{PM2} = \sum_{i=0}^{\infty} B_i e^{j2\pi(f_c \pm i \cdot f_2)t} \quad (2)$$

where A_i and B_i are the amplitude of the ith ($i = 0, 1, 2, \ldots$) comb-lines of the two combs, and f_c is the frequency of the light source. The optical signal after PM1 is modulated by a DPMZM that is driven by an LFM signal, of which the instantaneous frequency is:

$$f_{LFM}(t) = f_0 + kt \quad (0 \le t \le T) \quad (3)$$

where f_0 is the initial frequency, k is the chirp rate, and T is the temporal width. By properly biasing the DPMZM to let it work at the carrier-suppressed single sideband (CS-SSB) modulation mode [23], an optical frequency-swept comb can be obtained (point C in Fig. 2(b)), which can be expressed as:

$$E_{DPMZM} = \sum_{i=0}^{\infty} C_i e^{j2\pi(f_c \pm i \cdot f_1 - f_0 - kt)t} \quad (0 \le t \le T) \quad (4)$$

where C_i is the amplitude of the ith swept-frequency comb-line. After that, the outputs from PM2 and the DPMZM are combined by another optical coupler (OC2) to get the photonic radar reference signal (point D in Fig. 2(b)), which is expressed as:

$$E_{OC} = E_{PM2} + E_{DPMZM}$$
$$= \sum_{i=0}^{\infty} \left[C_i e^{j2\pi(f_c \pm i \cdot f_1 - f_0 - kt)t} + B_i e^{j2\pi(f_c \pm i \cdot f_2)t} \right],$$
$$(0 \leq t \leq T) \quad (5)$$

Next, the photonic radar reference signal is divided into two branches. The signal in the upper branch is sent to the transmitting array, which is composed of a wavelength division multiplexer (WDM), M photodetectors (PD), M power amplifiers (PA), and M transmitting antennas. The WDM is used to select out the mth, $(m = 1, 2, \ldots, M)$ optical sidebands from both of the two frequency combs. The obtained M-channel optical sideband pairs, as shown at point D in Fig. 2(b), are sent to M photodetectors (PDs), respectively, to realize optical-to-electrical conversions. In this way, M electrical LFM signals covering different frequency ranges are generated. With the assumption of $f_1 < f_2$, the instantaneous frequency of the mth radar signal is

$$f_m(t) = f_0 + kt + m\Delta f \quad (0 \leq t \leq T) \quad (6)$$

where $\Delta f = f_2 - f_1$ is the frequency difference between the two RF signals. Then, each LFM signal is amplified by a power amplifier (PA) before emitted to the air through a transmitting antenna. It should be noted that to make sure that the two optical sidebands corresponding to a specific transmitting channel can be selected out without interference, $(m - 1)f_2 < mf_1 - f_0 - kT$ should be satisfied. Meanwhile, $\Delta f \geqslant kT$ should be satisfied to avoid the spectral overlap between two LFM signals in adjacent transmitting channels.

Compared with the signal generation methods in previous microwave photonic MIMO radars, the proposed multi-band LFM signal generation by heterodyning two optical frequency combs has a simple and compact structure. The frequency and bandwidth of the generated LFM signals can be easily reconfigured by adjusting the frequencies of the electrical signals. Besides, the generated LFM signals in multiple channels are coherent, which is helpful to achieve precise target detection and imaging.

B. Photonics-Based MIMO Radar Echo Processing

The transmitted M orthogonal radar signals are scattered by the target, and the reflected echoes are collected by the receiving array with N receive antennas. Fig. 3 shows the structure of the photonic MIMO radar receiving array. The photonic radar reference signal is divided into N branches and sent to the N receivers, respectively. In the nth, $(n = 1, 2, \ldots, N)$ receiver, the echo signal is split into M branches to drive M Mach-Zehnder modulators (MZM), respectively. The reference signal passes through a WDM to separate the M optical sideband pairs, which are fed to M PDs to perform photonic frequency mixing. After
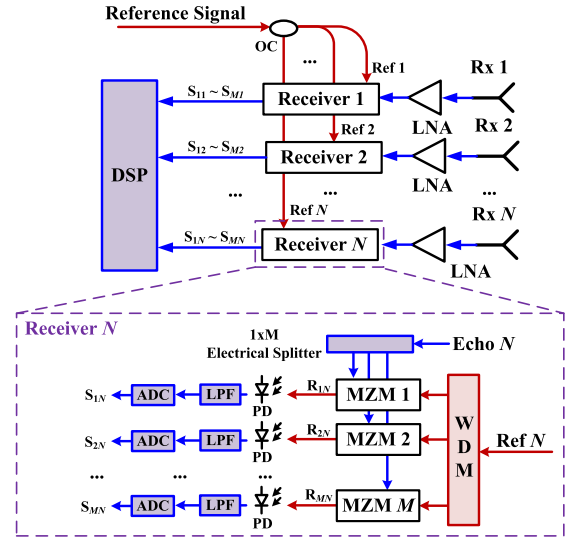

Fig. 3. The schematic diagram of the photonic MIMO radar receiving array. Rx: Receiving antenna, LNA: Low-noise amplifier, DSP: Digital signal processing, MZM: Mach Zehnder modulator, LPF: Low-pass filter, ADC: Analog-to-digital convertor.

each PD, a low-band pass filter is followed to get the de-chirped signal corresponding to the radar signal transmitted by the mth transmitter and received by the nth receiver (S_{mn}) [24]. Then, analog-to-digital converters (ADC) are used to sample the de-chirped signals from the M branches. This way, de-chirp processing and separation of the multi-channel radar echoes are implemented. The obtained $M \times N$ digital signals are processed by the digital processing unit.

For the proposed receiving array, the use of photonics-based de-chirp processing transfers the target information from broadband radar echoes to a low-frequency signal, which avoids the need for high-speed analog-to-digital conversions and enables fast signal processing. In each receiver, the processing is implemented in M parallel channels, which ensures the de-chirped signals of multiple channels can be separated without interferences from adjacent channels. If multiple laser sources with largely separated wavelengths are used, the system can be designed to use only one MZM in each receiver [21]. While, the number of channels may be limited in this case, considering the current commercial MZM usually has a wavelength-dependent response.

C. MIMO Array and Back Projection Imaging

Fig. 4 shows the microwave photonic MIMO radar array, which is a liner array with M transmitters and N receivers. The interval between two adjacent receiving antennas is set to d and the interval between two adjacent transmitting antennas is set to $N \cdot d$. According to the principle of phase center approximation (PCA) [25], the equivalent array is a uniform linear array (ULA) composed of $M \times N$ transmit-receive array elements with an element spacing of $d/2$, as shown in Fig. 4.

With the equivalent ULA, DBF algorithms can be applied to construct the image, as demonstrated in [16]. In this work, we chose the back projection (BP) imaging algorithm, which
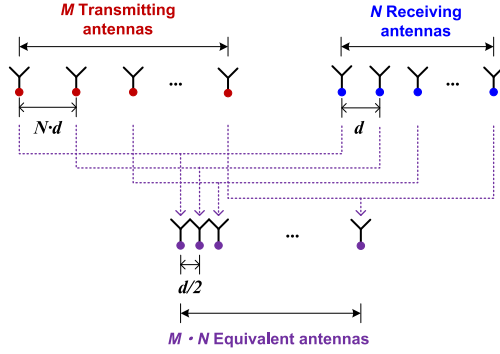
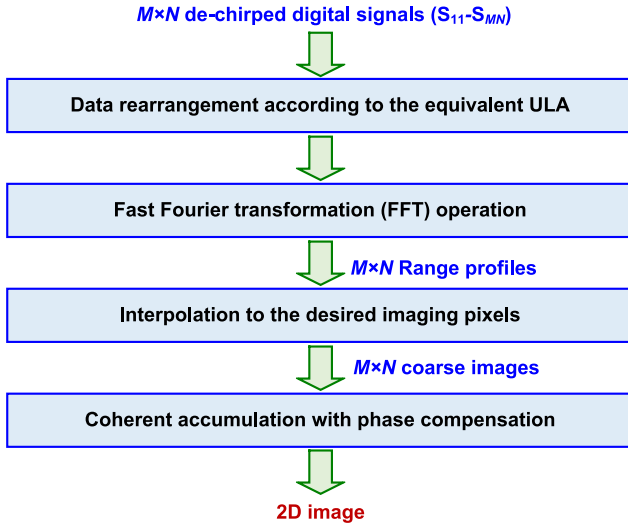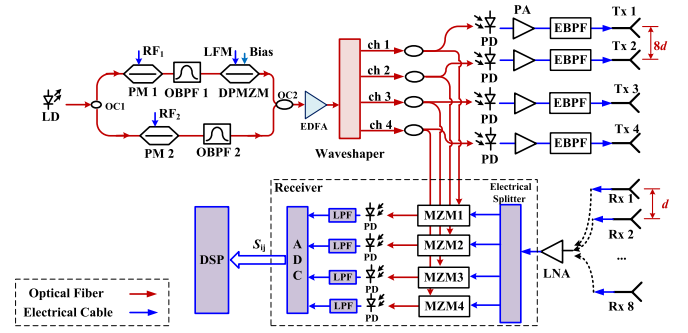Fig. 4. Design of the microwave photonic MIMO radar array.

Fig. 5. Signal processing flow chart of the microwave photonic MIMO radar imaging.

is a general imaging approach for high-precision imaging in arbitrary aperture geometries [26], [27]. Fig. 5 shows the signal processing flow chart of the microwave photonic MIMO radar imaging. First of all, the $M \times N$ de-chirped digital signals are rearranged to match the equivalent ULA. Then, $M \times N$ range profiles are acquired by performing fast Fourier transformation (FFT) to the $M \times N$ de-chirped digital signals [8]. Next, all the range profiles are interpolated to the desired imaging pixels, generating $M \times N$ coarse images. Finally, all the coarse images are coherently accumulated to get the final 2D image, in which phase compensation is performed [28]. The amplitude of the image pixel at the coordinate of (x_i, y_j) can be expressed as:

$$A_{\text{co}}(x_i, y_j) = \sum_{l=1}^{M \times N} R_l(t_{ij}) \exp \left(j \frac{4\pi t_{ij} c}{2\lambda_l} \right) \qquad (7)$$

where t_{ij} is the round-trip time delay between the lth equivalent array element ($l = 1, 2, \ldots, M \times N$) and the image pixel at (x_i, y_j), c is the speed of light, and λ_l is the center wavelength of the radar signal for the lth array element. It should be noted that, when performing BP imaging based on Eq. (7), the factor of the phase compensation depends on the center wavelength of the corresponding radar signal because the center wavelengths

Fig. 6. Experiment setup of the 4×8 microwave photonic MIMO radar.

of the multiple transmitting channels are largely separated. This is different from narrow-band BP imaging, in which the phase compensation is calculated with a fixed central wavelength.

The range resolution (R_{res}) and azimuth resolution (θ_{ress}) of BP imaging are determined by the radar bandwidth and the size of the equivalent radar aperture [16], respectively, i.e.,

$$R_{res} = \frac{c}{2B} \qquad (8)$$

$$\theta_{res} = \frac{\lambda_0}{2\pi D} \cdot 180° \qquad (9)$$

where B and D are the bandwidth of the radar system and the size of the equivalent aperture, respectively, and λ_0 is the center wavelength of the radar signal.

III. EXPERIMENT AND RESULTS

A. Generation of the Orthogonal LFM Signals

To verify the feasibility of the proposed microwave photonic MIMO radar, an experiment is carried out. A 4×8 microwave photonic MIMO radar is established, of which the setup is shown in Fig. 6. Limited by the hardware constraints, the eight receiving antennas share the same receiver by collecting the radar echoes in a time-division manner, which is feasible for the detection of static and low-speed targets. In the experiment, the CW light source generated by an LD (TeraXion NLL04) at 1549.72 nm with a power of 17 dBm is split into two branches by an optical coupler. In the upper branch, the light is modulated by an RF signal with a frequency of 30 GHz through PM1 to generate an optical frequency comb. An OBPF (OBPF1: Yenista XTM-50) is used to select out four comb lines and the optical spectrum is shown in Fig. 7(a), which is measured by an optical spectrum analyzer (Yokogawa AQ6370C) with a resolution of 0.02 nm. The obtained optical frequency comb is sent to a DPMZM (Fujitsu FTM7962EP, Bandwidth: 22 GHz) driven by an LFM signal generated by an arbitrary waveform generator (Keysight 8195A). The LFM signal has a frequency range of 16–18 GHz, a repetition rate of 100 kHz, and a duty ratio of 90%. By adjusting the bias voltages, the DPMZM works at the SSB modulation mode, and Fig. 7(b) shows the spectrum of the obtained frequency-swept optical frequency comb, in which the optical carrier is suppressed by 18 dB after SSB modulation. Meanwhile, the light from the lower branch of OC1 is sent to another PM (PM2) that is driven by a 32-GHz radio frequency
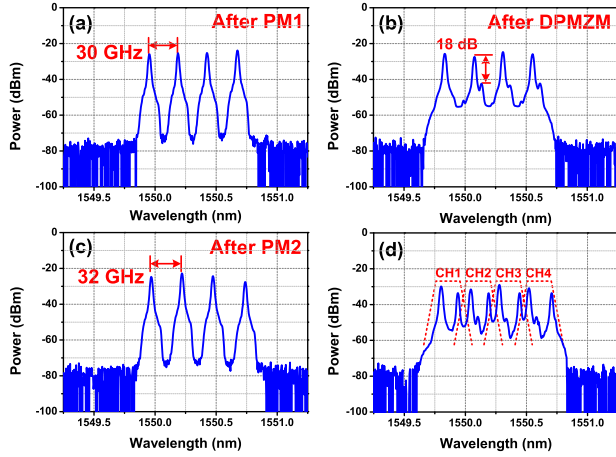
Fig. 7. The spectra of the optical frequency comb after (a) OBPF1 and (c) OBPF2, the spectra of (b) The frequency-swept optical frequency comb after the DPMZM, and (d) The combined optical signal.

signal, generating an optical frequency comb with a fixed FSR of 32 GHz. An optical filter (OBPF2) is followed to select the corresponding comb lines, of which the optical spectrum is shown in Fig. 7(c). Then, the optical signals in the two branches are combined by OC2 and amplified by an EDFA (Amonics Ltd.) with a gain of ∼20 dB. The optical spectrum of the obtained signal is shown in Fig. 7(d).

Next, the optical signal is sent to a Waveshaper (Finisar, 4000s), which works as a WDM with its filtering characteristics shown in Fig. 7(d). The optical signal from each output channel of the Waveshaper is equally split into two branches by an OC, and the signals in the two branches are sent to the transmitting array and receiving array, respectively. In the transmitting array, four PDs (u2tXPDV2120RA; bandwidth: 40 GHz) are used to perform optical-to-electrical conversion, generating four LFM signals in different frequency bands. An electrical spectrum analyzer (ESA, R&S FSV40) with a resolution bandwidth (RBW) of 200 kHz is used to measure electrical spectra of the generated four LFM signals, as shown in Fig. 8(a), (c), (e), and (g), respectively. The waveforms in a single period are also shown in the insets, which are measured by a real-time oscilloscope (Keysight DSO-X 92504A) with a sampling rate of 80 GSa/s. The time-frequency relationships obtained by performing short-time Fourier transform (STFT) to the sampled waveforms are plotted in Fig. 8(b), (d), (f), and (h), respectively. As can be seen, four LFM signals covering the frequency bands of 18–20 GHz, 20–22 GHz, 22–24 GHz, and 24–26 GHz are successfully generated. The signal-to-noise and distortion ratio (SINAD) of the four LFM signals is about 37 dB. Each LFM signal is amplified by an electrical amplifier (Agilent 83020A) and passed through an electrical bandpass filter (EBPF) before launched to the air through a K-band antenna (Operation bandwidth: 18-26.5 GHz; Gain: 20 dBi).

B. Antenna Distribution and MIMO Radar Signal Reception

Fig. 9 shows the MIMO antenna array distribution used in the experiment. The spacing between two adjacent receiving
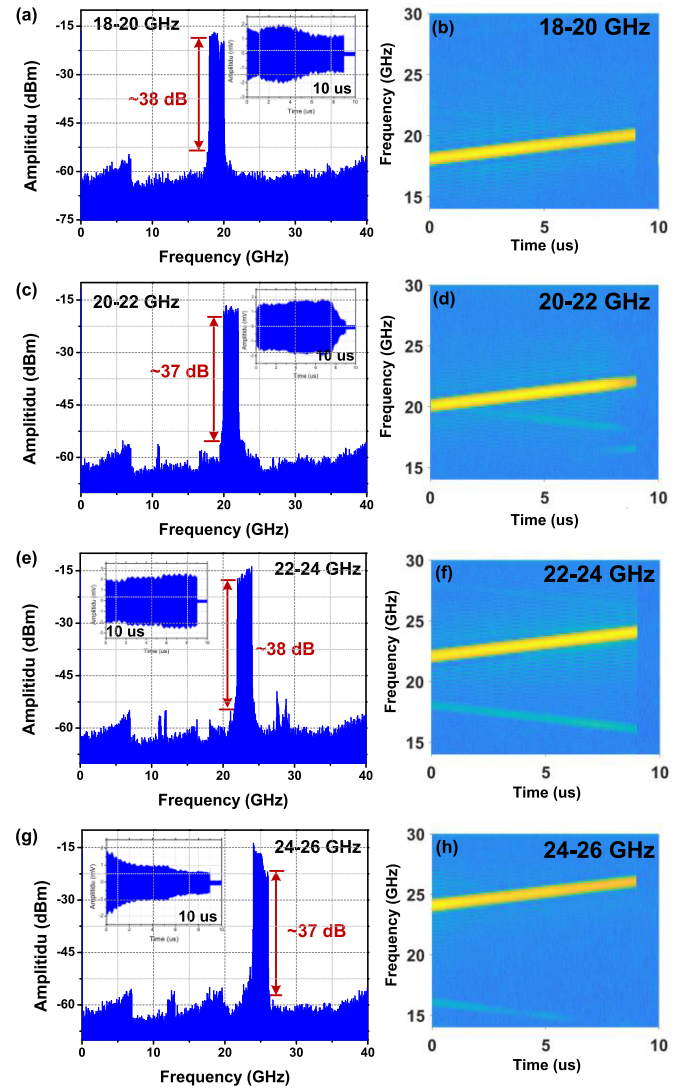

Fig. 8. The waveform and spectrum of the generated LFM signal in (a) 18–20 GHz, (c) 20–22 GHz, (e) 22–24 GHz, (g) 24–26 GHz; and the time-frequency response curves of the generated LFM signals with the frequency of (b) 18–20 GHz, (d) 20–22 GHz, (f) 22–24 GHz, (h) 24–26 GHz.
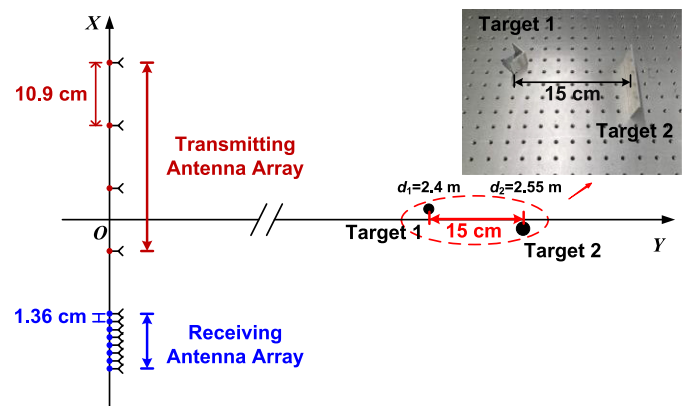

Fig. 9. The distribution of the antenna array and targets in the experiment. (inset: Picture of the targets).

antennas is 1.36 cm, which equals the center wavelength from 18 GHz to 26 GHz. The interval between two adjacent transmitting antennas is set to 10.9 cm, eight times the spacing between adjacent receiving antennas. In this case, the 4×8 MIMO array is equivalent to a 32-element ULA with an element spacing of 0.68 cm. In our experiment, a single receiver is established to collect the radar echoes in the eight receiving positions in turn. In each receiving position, the radar echoes collected by an antenna are amplified by a low-noise amplifier (LNA, CONNPHY), and then equally split into four channels to modulate four optical reference signals at four MZMs (Fujitsu FTM7938, bandwidth: 28 GHz), respectively. The output optical signals are sent to four PDs to perform photonic de-chirping, and an LPF with a bandwidth of 100 MHz is used after each PD to select the required de-chirped signals. The four de-chirped signals are sampled simultaneously by a four-channel real-time oscilloscope (Agilent, DS09404A) working at a sampling rate of 200 MSa/s in each channel. In this way, 32 de-chirped signals (S_{ij}) corresponding to the ith transmitter and the jth receiver ($i = 1, 2, 3, 4$; $j = 1\,2\,3\,4\,5\,6\,7\,8$) of the 4×8 MIMO radar are obtained.

To check the signal reception capability of the established microwave photonic MIMO radar, detection of two reflectors with different sizes is performed. One of the targets is a corner reflector with a size of 3.3 cm $\times$ 3.3 cm $\times$ 3.3 cm, and the other one is a metallic plane with a size of 6.5 cm $\times$ 4.5 cm. The two targets are placed at a distance of 2.4 m and 2.55 m from the antenna array, respectively, as shown in Fig. 9. Figs. 10(a)–(d) show the sampled waveforms of the de-chirped signals (S_{11}, S_{21}, S_{31}, and S_{41}) in a temporal period of 10 us. After performing FFT, the range profiles are obtained and shown in Figs. 10(e)-(h), respectively. As can be seen, two peaks corresponding to the two targets are observed, of which the measured distances marked in each range profile deviate by less than 2 cm from the real values, and the average SINAD of the four range profiles is about 13 dB. Here, due to the different observation angles in obtaining the four range profiles, the amplitude distributions of targets in Figs. 10(e)-(h) are also different. These results can confirm that the de-chirping and separation of radar echoes from the four transmitting channels are successfully implemented.

C. Microwave Photonic MIMO Radar Imaging

For the targets shown in Fig. 9, the 2D image constructed by the BP algorithm with 512×512 pixels is shown in Fig. 11(a), in which two bright spots, corresponding to the two targets, appear at the ranges of 2.4 m and 2.551 m, respectively. Based on Eq. (8) and Eq. (9), the theoretical range resolution and theoretical azimuth resolution are 7.5 cm and 1.85°, respectively. Figs. 11(b) and (c) show the range profile and azimuth profile along the image center of target 1 (Range=2.40 m; Azimuth= 0.05 m), respectively. In Fig. 11(b), the full width at half maximum (FWHM) of the range peak for target 1 is 7.67 cm, which is very close to the theoretical range resolution. This indicates that target 1 can be seen as a point target in the range direction because it has smaller size in range direction than the theoretical range resolution. In Fig. 11(c), the FWHM of the azimuth peak
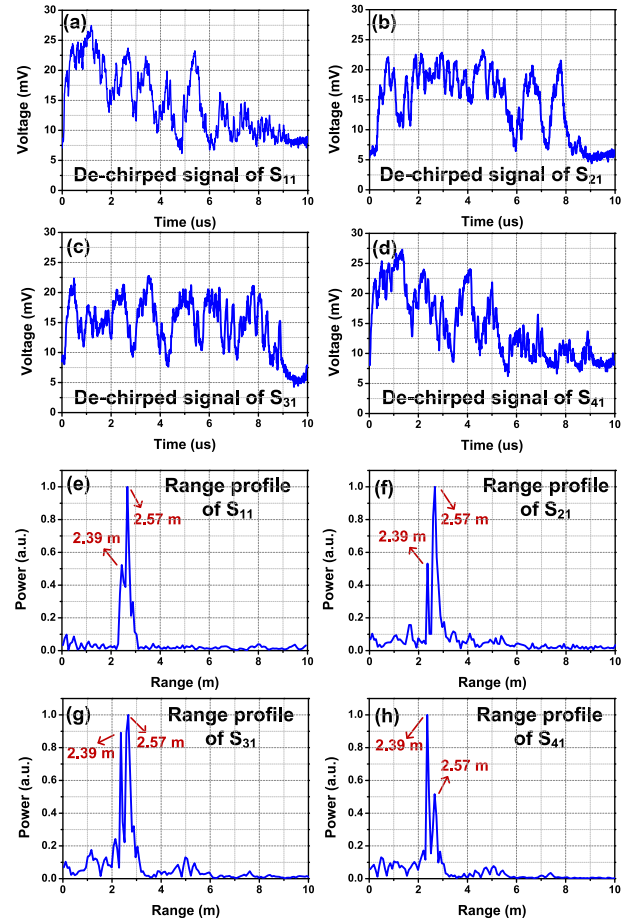

Fig. 10. The sampled waveform of the de-chirped signal (a) S_{11}, (b) S_{13}, (c) S_{15}, and (d) S_{17}, and the corresponding range profiles are shown in (e), (f), (g), and (h), respectively.

is 9.16 cm, corresponding to an azimuth angle of 2.18°. Here, target 1 covers a distance of $\sim$4.7 cm in the azimuth direction, which can not be ignored compared with the theoretical azimuth resolution ($\sim$7.7 cm) at the range of 2.4 m. Thus, the measured azimuth peak in Fig. 11(c) is broadened compared with the real azimuth distance.

Finally, five corner reflectors having the same size as target 1 in Fig. 9 are used as the targets to demonstrate the imaging of multiple targets. The five corner reflectors are arranged to form a triangle shape, as shown in Fig. 12(a). The constructed BP image is shown in Fig. 12(b). As can be seen, the five reflectors are observed in the obtained image with their distributions close to the real scene. The background noises in Fig. 12(b) are mainly attributed to the time-division data sampling for different receiving positions, which introduces possible phase noises to different receiving channels. In practical applications with simultaneous reception of the multiple channels, the background noises will be well suppressed. It is also found that the image spot corresponding to reflector 1 is broadened compared with the other reflectors. This is caused by the fact that reflector 1 is sheltered by the other reflectors from the radar array and the reduced equivalent aperture size for observing reflector 1 results in a degraded azimuth resolution. In spite of these defects, the
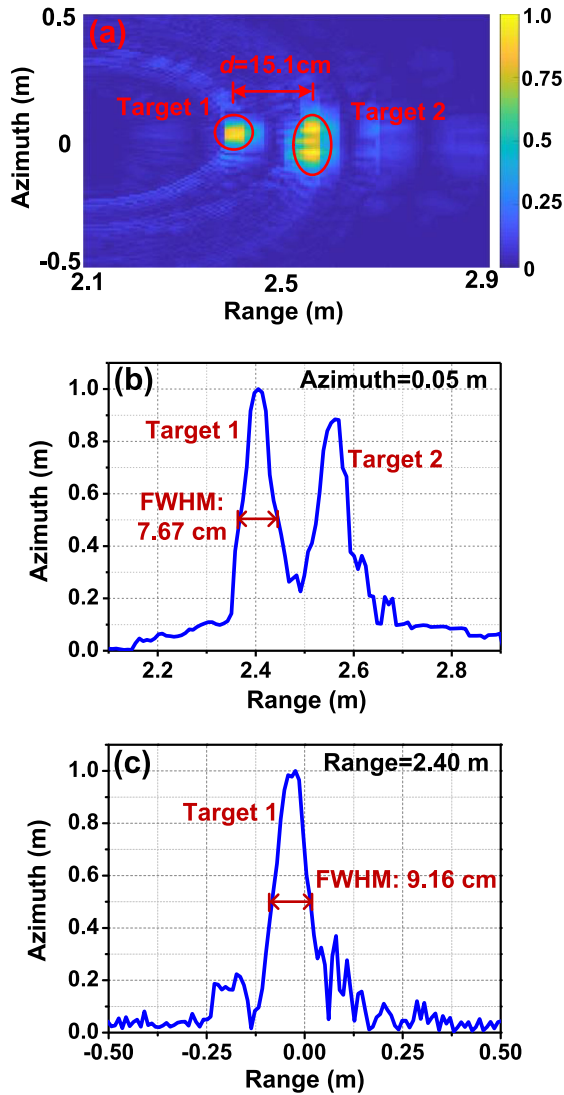
Fig. 11. The image results by (a) the coherent BP algorithm, and the profiles of the PSF along the (b) range direction (Azimuth = 0.05 m), and (c) Azimuth direction (range= 2.40 m).

imaging result in Fig. 12 can still confirm the high-resolution imaging capability of the microwave photonic MIMO radar.

IV. CONCLUSION

In conclusion, we have demonstrated a microwave photonic MIMO radar for high-resolution imaging. The proposed radar uses photonic technology to have a large operation bandwidth and MIMO technology to form a large equivalent aperture size, enabling high-resolution radar imaging in both range and azimuth directions. A microwave photonic 4×8 MIMO radar with a 2-GHz bandwidth in each channel is established, and high-resolution radar imaging with BP algorithm is demonstrated. The experimental result not only verifies the feasibility of the multi-channel radar signal generation and processing, but also confirms the capability for high-resolution imaging. While, since the microwave photonic MIMO radar convers a large frequency range, the wideband frontend may suffer from
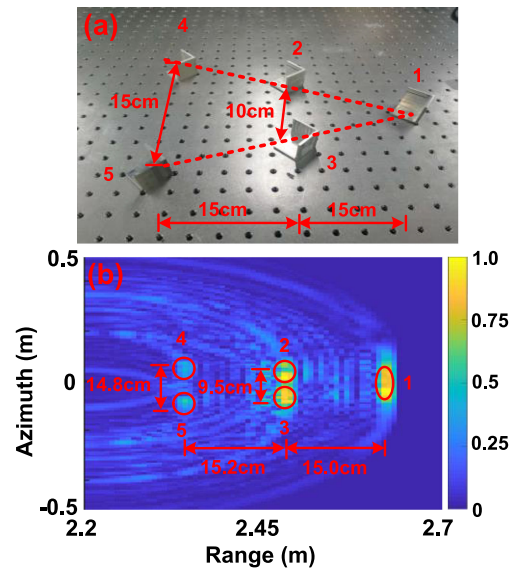

Fig. 12. (a) Picture of the multiple targets in the experiment, and (b) the BP imaging result.

reduced performance in terms of noise figure, launched power, and receiver sensitivity, compared with traditional narrow-band MIMO radar. Besides, the frequency dependent radar cross section (RCS) of the target is not considered in our experiment. If a calibration is adopted to deal with this problem, the imaging performance is expected to be improved.

REFERENCES

[1] J. Yao, "Microwave Photonics," *J. Lightw. Technol.*, vol. 27, no. 3, pp. 314–335, 2009.
[2] J. Capmany and D. Novak, "Microwave photonics combines two worlds," *Nat. Photon.*, vol. 1, no. 6, pp. 319–330, 2007.
[3] A. Seeds and K. Williams, "Microwave photonics," *J. Lightw. Technol.*, vol. 24, no. 12, pp. 4628–4641, Dec. 2006.
[4] S. Pan and Y. Zhang, "Microwave photonic radars," *J. Lightw. Technol.*, vol. 38, no. 19, pp. 5450–5484, 2020.
[5] D. Grodensky, D. Kravitz, and A. Zadok, "Ultra-wideband microwave-photonic noise radar based on optical waveform generation," *IEEE Photon. Technol. Lett.*, vol. 24, no. 10, pp. 839–841, May 2012.
[6] Y. Yao, F. Zhang, Y. Zhang, X. Ye, D. Zhu, and S. Pan, "Demonstration of ultra-high-resolution photonics based Ka-band inverse synthetic aperture radar imaging," in *Opt. Fiber Commun. Conf.*, Paper Th3G.5.
[7] P. Ghelfi *et al.*, "A fully photonics-based coherent radar system," *Nature*, vol. 507, no. 7492, pp. 341–345, 2014.
[8] F. Zhang, Q. Guo, Z. Wang, P. Zhou, G. Zhang, J. Sun, and S. Pan, "Photonics-based broadband radar for high-resolution and real-time inverse synthetic aperture imaging," *Opt. Exp.*, vol. 25, no. 14, pp. 16274–16281, 2017.
[9] S. Peng *et al.*, "High-resolution W-band ISAR imaging system utilizing a logic-operation-based photonic digital-to-analog converter," *Opt. Exp.*, vol. 26, no. 2, pp. 1978–1987, 2018.
[10] R. Li *et al.*, "Demonstration of a microwave photonic synthetic aperture radar based on photonic-assisted signal generation and stretch processing," *Opt. Exp.*, vol. 25, no. 13, pp. 14334–14340, 2017.
[11] J. Shi, F. Zhang, D. Ben, and S. Pan, "Simultaneous radar detection and frequency measurement by broadband microwave photonic processing," *J. Lightw. Technol.*, vol. 38, no. 8, pp. 2171–2179, Apr. 2020.
[12] Y. Tong *et al.*, "Photonics-based coherent wideband linear frequency modulation pulse signal generation," *Opt. Lett.*, vol. 43, no. 5, pp. 1023–1026, 2018.
[13] C. Ma *et al.*, "Microwave photonic imaging radar with a sub-centimeter-level resolution," *J. Lightw. Technol.*, vol. 38, no. 18, pp. 4948–4954, Sep. 2020.

[14] G. Sun, F. Zhang, S. Pan, and X. Ye, "Frequency-domain versus time-domain imaging for photonics-based broadband radar," *Electron. Lett.*, vol. 56, no. 24, pp. 1330–1332, 2020.

[15] S. Pan, X. Ye, Y. Zhang, and F. Zhang, "Microwave photonic array radars," *IEEE J. Microw.*, vol. 1, no. 1, pp. 176–190, Jan. 2021.

[16] B. Gao, F. Zhang, E. Zhao, D. Zhang, and S. Pan, "High-resolution phased array radar imaging by photonics-based broadband digital beamforming," *Opt. Exp.*, vol. 27, no. 9, pp. 13194–13203, 2019.

[17] I. Bekkerman and J. Tabrikian, "Target detection and localization using MIMO radars and sonars," *IEEE Trans. Signal Process.*, vol. 54, no. 10, pp. 3873–3883, Oct. 2006.

[18] S. Maresca *et al.*, "Coherent dual-band 2x4 MIMO radar experiment exploiting photonics," presented at the 2020 XXXIIIrd Gen. Assem. Sci. Symp. Int. Union Radio Sci., Rome, Italy, Aug./Sep. 2020.

[19] X. Xiao, S. Li, S. Peng, D. Wu, X. Xue, X. Zheng, and B. Zhou, "Photonics-based wideband distributed coherent aperture radar system," *Opt. Exp.*, vol. 26, no. 26, pp. 33783–33796, 2018.

[20] J. Dong, F. Zhang, Z. Jiao, Q. Sun, and W. Li, "Microwave photonic radar with a fiber-distributed antenna array for three-dimensional imaging," *Opt. Exp.*, vol. 28, no. 13, pp. 19113–19125, 2020.

[21] F. Zhang, B. Gao, and S. Pan, "Photonics-based MIMO radar with high-resolution and fast detection capability," *Opt. Exp.*, vol. 26, no. 13, pp. 17529–17540, 2018.

[22] F. Berland *et al.*, "Microwave photonic MIMO radar for short-range 3D imaging," *IEEE Access*, vol. 8, pp. 107326–107334, Jun. 2020.

[23] Y. M. Zhang and S. L. Pan, "A photonics-based multi-function analog signal processor based on a polarization division multiplexing Mach-Zehnder modulator," *Opt. Lett.*, vol. 42, no. 23, pp. 5034–5037, 2017.

[24] F. Zhang, Q. Guo, and S. Pan, "Photonics-based real-time ultra-high-range-resolution radar with broadband signal generation and processing," *Sci. Rep.*, vol. 7, 2017, Art. no. 13848.

[25] A. Bellettini and M. A. Pinto, "Theoretical accuracy of synthetic aperture sonar micronavigation using a displaced phase-center antenna," *IEEE J. Ocean. Eng.*, vol. 27, no. 4, pp. 780–789, Oct. 2002.

[26] S. Ozsoy and A. A. Ergin, "Pencil back-projection method for SAR imaging," *IEEE Trans. Image Process.*, vol. 18, no. 3, pp. 573–581, Mar. 2009.

[27] C. Jakowatz, D. Wahl, and D. Yocky, "Beamforming as a foundation for spotlight-mode SAR image formation by backprojection," in *Proc. SPIE-Algorithms Synth. Aperture Radar Imag.*, Mar. 2008, Art. no. 69700Q.

[28] G. Sun and F. Zhang, "Convolutional neural network (CNN)-based fast back projection imaging with noise-resistant capability," *IEEE Access*, vol. 8, pp. 117080–117085, Jun. 2020.